Nanoscale Advances

ROYAL SOCIETY OF CHEMISTRY

PAPER

View Article Online
View Journal | View Issue

Cite this: *Nanoscale Adv.*, 2024, **6**, 4885

Biosynthesis of ZnO nanoparticles using aqueous extracts of *Eclipta prostrata* and *Piper longum*: characterization and assessment of their antioxidant, antibacterial, and photocatalytic properties†

Xuan Thanh Tran,[a] Thanh Thi Lan Bien,[a] Thuan Van Tran *[b] and Thuy Thi Thanh Nguyen*[a]

Chemical syntheses of nanoparticles that release toxic substances into the environment rarely meet the strict requirements of green chemistry principles. Instead, green synthesis of nanoparticles using plant extracts brings a safe, rapid, and effective process, contributing to solving environmental pollution problems. Here, we report the green synthesis of multifunctional ZnO nanoparticles (ZnONPs) using aqueous extracts of *E. prostrata* leaves and *P. longum* fruits. The XRD results affirmed the existence of hexagonal crystalline ZnONPs with particle sizes of 17–30 nm. The optical analysis revealed bandgap energies of 3.10 eV and 3.16 eV for ZnONPs biosynthesized using *E. prostrata* and *P. longum* extracts, respectively. The synthesized ZnONPs showed potential antioxidant activity through DPPH and ABTS methods. Among the antibacterial outcomes against pathogenic bacterial strains (*S. aureus*, *B. cereus*, *E. coli*, and *S. typhimurium*), ZnONPs exhibited the highest zone of inhibition (18.5 mm) for *S. aureus*. Moreover, both ZnONPs biosynthesized using *E. prostrata* and *P. longum* extracts served as strong photocatalysts in the degradation of crystal violet with degradation efficiencies of 95.64% and 99.90%, respectively. Therefore, biosynthesized ZnONPs hold significant promise as antioxidants, antibacterial agents, and photocatalysts.

Received 19th April 2024
Accepted 19th July 2024

DOI: 10.1039/d4na00326h

rsc.li/nanoscale-advances

1 Introduction

Currently, nanoparticles (NPs) are garnering significant attention across various domains, including catalysis, electronics, and biomedical sciences, due to their tiny size and high surface area.[1] Notably, metal oxide (M–O) NPs are widely acknowledged for their versatile applications such as sensors, catalysts, antimicrobial agents, cosmetics, and energy storage devices.[2–4] Among these NPs, zinc oxide nanoparticles (ZnONPs) exhibit exceptional optical, semiconducting, antifungal, antioxidant, and antibacterial properties.[5,6] ZnONPs possess a wide band gap, high chemical stability, a high electron transfer rate, biocompatible substances and minimal toxicity.[7] Importantly, ZnONPs have been recognized as a safe metal oxide by the US Food and Drug Administration (FDA). Consequently, ZnONPs can be adopted as antioxidant and antibacterial agents in surface coatings for food containers and within biological systems.[8]

Various methods, including chemical precipitation,[9] physical vapor deposition,[10] hydrothermal,[11] sol–gel,[12] ultrasound-assisted,[13] thermal decomposition,[14] green synthesis,[15] microwave-assisted,[16] ball milling,[17] and others, have been employed for synthesizing ZnONPs. Among these approaches, green synthesis has attracted considerable attention for its ability to overcome the limitations of conventional chemical and physical synthesis of NPs, such as the use of expensive and toxic chemicals, dependence on specialized equipment, and the substantial generation of chemical waste that can harm the environment and impact application areas.[18] By contrast, the use of green synthesis offers advantages such as cost-effectiveness, the generation of non-toxic byproducts, ease of scaling up for large-scale production, and improved biocompatibility, particularly in clinical applications.[19]

Different parts of plants (leaves, flowers, roots, *etc.*) are available in phytochemicals and biomolecules, including polyphenols, flavonoids, alkaloids, saponin, terpenoids, amino acids, proteins, tannins, and glycosides.[20,21] These compounds play a crucial role in reducing metal ions and acting as capping

[a]*Nong Lam University Ho Chi Minh City, Ho Chi Minh City 700000, Vietnam. E-mail: nguyenthanhthuy@hcmuaf.edu.vn*

[b]*Institute of Environmental Technology and Sustainable Development, Nguyen Tat Thanh University, 298-300A Nguyen Tat Thanh, District 4, Ho Chi Minh City 755414, Vietnam. E-mail: tranvt@ntt.edu.vn; tranuv@gmail.com*

† Electronic supplementary information (ESI) available. See DOI: https://doi.org/10.1039/d4na00326h

agents to minimize nanoparticle aggregation, making them ideal candidates for the green synthesis of zinc oxide nanoparticles (ZnONPs).[20,21] This method is noted for its ease of synthesis, affordability, and safety.

Recent studies have utilized the *C. jambhiri* Lush. leaf extract to prepare ZnONPs for investigating their photocatalytic applications.[22] Extracts of leaves from *C. reticulata*,[23] and *P. pinnata*[24] have been employed for the synthesis of ZnONPs. The bacterial and photocatalytic activities of the resulting ZnONPs were also studied. Indeed, Venkatesan *et al.*[25] reported the preparation ZnONPs using *E. milii* leaf constituents to catalyze the decomposition of methylene blue under direct solar light irradiation. Additionally, ZnONPs synthesized using leaf extracts from two medicinal species, *C. fistula* and *M. azedarach,* demonstrated bactericidal applications against two clinical strains of *S. aureus* and *E. coli*.[26]

False daisy, scientifically identified as *Eclipta prostrata* L. and a member of the Asteraceae family, is commonly grown in tropical and subtropical regions such as Asia and Africa. This versatile herb features multiple branches, reaching heights of about 20–90 cm, and strigose leaves measuring approximately 2.2–8.5 cm long. The flowers are white or yellow and arranged in compact clusters. *E. prostrata* has been utilized in ancient healing traditions to address various conditions such as loose teeth, hemorrhagic, hepatic and renal issues, whitening of hair, dizziness, diabetes, respiratory problems, tuberculosis and more.[27] *E. prostrata* yields a diverse range of chemical compounds, including alkaloids, flavonoids, steroids, saponins, alkenynes, triterpenes, polyacetylenes, polypeptides and carbohydrates, all of which have been successfully isolated and identified.[28]

Piper longum L., belonging to the Piperaceae family, is predominantly cultivated for its fruits and grows across India, Indonesia, Brazil, Philippines, Myanmar, Vietnam, Thailand, and other regions.[29] These plants are traditionally valued for their anticancer, spasmolytic, antidiabetic, anti-inflammatory, antimicrobial, hepatoprotection and cardioprotection properties. They are commonly used to treat conditions such as cough, constipation, stomachache, asthma and spleen-related diseases.[30] The oblong, blunt and blackish-green *P. longum* fruits, measuring approximately 2.5–3.5 cm in length and 5 mm in thickness, showcase a spectrum of pharmacological activities.[31] These include anticancer, anti-inflammatory, antimicrobial, antioxidant, immunomodulatory, larvicidal, hepatoprotective, antiplatelet, antihyperlipidemic, and antifungal properties.[32] They contain numerous alkaloids such as rosin, piperchabaoside, guineensine, and piperlongumine, alongside compounds like lignans, esters, volatile oils, proteins, tannins, saponins, amino acids, phenols, starch, and carbohydrates.[33,34] Due to the presence of these constituents, both *E. prostrata* and *P. longum* extracts play a pivotal role in bioreducing metal ions to nano-scale dimensions and acting as capping agents for nanoparticles. This capability is critical for achieving stability and biocompatibility in nanoparticle synthesis. Moreover, their rich chemical composition and associated medicinal benefits highlight their potential for efficient green synthesis of nanoparticles.

The primary objective of this study is to propose an eco-friendly and effective approach to synthesize ZnONPs using plant extracts from *E. prostrata* and *P. longum* as natural reducing and capping agents. The prepared ZnONPs underwent a detailed investigation to assess their structural, vibrational, optical, morphological, zeta potential, compositional, and band-gap properties through analytical techniques. Furthermore, the antibacterial activity of the synthesized ZnONPs was assessed against four bacterial strains: *S. aureus*, *B. cereus*, *E. coli*, and *S. typhimurium*. Additionally, the photocatalytic activity of ZnONPs was investigated by studying their ability to degrade an organic pollutant, specifically crystal violet dye. This study contributes to the green chemistry field by demonstrating the potential of plant extracts in the fabrication of multi-functional ZnONPs for wastewater treatment and biomedical engineering.

2 Materials and methods

2.1. Materials and characterization

Chemicals, raw materials (*E. prostrata* and *P. longum*), bacterial strains, and characterization are detailed in the ESI.†

2.2. Preparation of aqueous plant extracts

E. prostrata and *P. longum* were cleaned using distilled water to eliminate undesired impurities. The raw precursors were dried at 50 °C using an air drier to remove moisture. Then, the dried plants were finely ground using an electric mixer. For the extraction process, 2 g of the prepared powder was immersed in 100 mL distilled water and the mixture was magnetically agitated at 60 °C in 1 h. Subsequently, the mixture was filtered through Whatman No. 1 filter paper and the resulting supernatant was stored at 4 °C for further experiments.

2.3. Synthesis of ZnONPs using aqueous extracts of *E. prostrata* and *P. longum*

The green ZnONPs were fabricated based on a method published in a previous study.[35] Initially, 80 mL of 0.1 M $Zn(CH_3COO)_2$ solution was combined with 30 mL of the aqueous extract of *E. prostrata* or *P. longum*. The resulting solution underwent stirring for 120 min at 80 °C. Subsequently, the pH of this mixture was adjusted to 7 using a 2 M NaOH solution and stirred continuously at 80 °C for another 60 min. Following this, centrifugation at 5000 rpm was carried out for 30 min to isolate the precipitate. This solid was then washed with deionized water and ethanol and then air-dried at 80 °C for 12 h. Finally, the obtained samples using *E. prostrata* or *P. longum* extract were calcined at 500 °C for 4 h in an air environment, denoted as ZnO_EPE and ZnO_PLE, respectively. The flow chart for the synthesis of ZnONPs is thoroughly described in Fig. 1.

2.4. Antibacterial, antioxidant, and photocatalytic activities of ZnONPs

Antibacterial, antioxidant, and photocatalytic activities of ZnONPs are described in the ESI.†

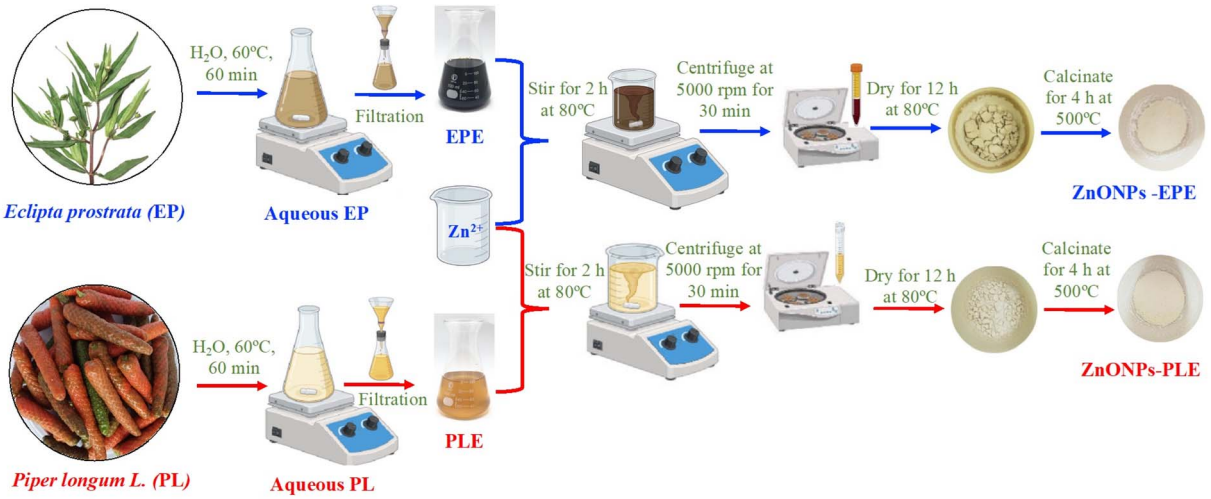

Fig. 1 Schematic representation of green synthesis of ZnONPs.

3 Results and discussion

3.1. Phytochemical test and the mechanism for green synthesis of ZnONPs

The role of phytochemicals derived from extracts of *E. prostrata* and *P. longum* in the reduction and stabilization of ZnONPs was assessed using qualitative analysis methods. The results in Table 1 showcase the presence of flavonoids, saponins, steroids, phenolics, and tannins in the *E. prostrata* extract, while the *P. longum* extract contains alkaloids, flavonoids, saponins, phenolics, terpenoids, and tannins. Furthermore, the phenolic and flavonoid contents of the aqueous extracts of *E. prostrata* and *P. longum* were determined using the quantitative analysis method, as shown in Table 2. The results indicate that the phenolic content in the *E. prostrata* extract (37.72 mg GAE per g) was higher than that in the *P. longum* extract (20.83 mg GAE per g). A similar trend is observed for flavonoid content, with the total content of flavonoids (20.83 mg QE per g) in the *E. prostrata* extract being higher than that in the *P. longum* extract (5.82 mg QE per g).

The precise mechanism of ZnONP production using the plant extracts remains incompletely understood, presenting a notable challenge for academic societies. At present, phytochemicals play an important role as reducing, capping and stabilizing agents in the synthesis of metal oxide nanoparticles, thereby controlling their size. In this study, the presence of phenolics, alkaloids, tannins and flavonoids containing –OH and $-NH_2$ groups in the *E. prostrata* and *P. longum* extracts facilitates the formation of ZnONPs.[36] The proposed mechanism for the formation of ZnONPs involves three main stages, as illustrated in Fig. 2. Firstly, the phytochemicals in the *E. prostrata* or *P. longum* extracts act as chelating agents, forming stable complexes with Zn^{2+} ions. Secondly, a hydrolysis reaction transforms these complexes into $Zn(OH)_2$. Thirdly, calcination is employed to remove the phytochemicals and convert $Zn(OH)_2$ into ZnO, initiating a growth phase through electrostatic interaction, leading to the formation of ZnONPs.

Table 1 Phytochemical screening of *E. prostrata* leaf and *P. longum* fruit extracts

	Results[a]	
Phytochemicals	*E. prostrata* extract	*P. longum* extract
Alkaloids	–	+++
Anthocyanins	–	–
Flavonoids	+++	++
Glycosides	–	–
Saponins	+++	–
Steroid	++	–
Phenolic compound	+++	++
Terpenoid	–	++
Tannins	+++	+++

[a] (+++): indicates high intensity, (++) indicates medium intensity, (+) indicates presence, and (–) absence of phytochemical constituents.

3.2. Effect of pH and $[Zn^{2+}]$

The formation of ZnONPs is remarkably reliant on pH, which changes the electrical charges of biochemical compounds present in the plant extract. This modification may alter their ability to reduce, cap and stabilize, consequently influencing the growth of the nanoparticles.[37] The formation of ZnONPs in the presence of either the *E. prostrata* leaves or *P. longum* fruit extract was conducted across a pH range of 7–10. Fig. 3 illustrates the XRD pattern of the ZnONPs synthesized through the green process, depicting pH changes during the ZnO nanoparticle synthesis. The diffraction peaks of ZnO_EPE conducted at pH 7 were observed at 32.13°, 34.78°, 36.61°, 47.88°, 56.94°, 63.20°, 66.72°, 68.28°, 69.40°, 72.88°, and 77.30°. Additionally, ZnO_EPE peaks for pH 8 exhibited diffraction angles (2θ) of 32.01°, 34.66°, 36.48°, 47.77°, 56.82°, 63.09°, 66.63°, 68.17°, 69.29°, 72.79°, and 77.19°. Similarly, the peaks of ZnO_EPE at pH 9 were positioned at 32.09°, 34.74°, 36.57°, 47.86°, 56.91°,

Table 2 The amount of the phenolic and flavonoid compounds in the aqueous extracts of *E. prostrata* leaf (EPE) and *P. longum* fruit (PLE). Abbreviations: GAE, gallic acid equivalents; QE, quercetin equivalents

Sample	Phenolic compounds (mg GAE per each gram of the sample)	Flavonoid compounds (mg QE per each gram of the sample)
EPE	37.72	20.83
PLE	15.23	5.82

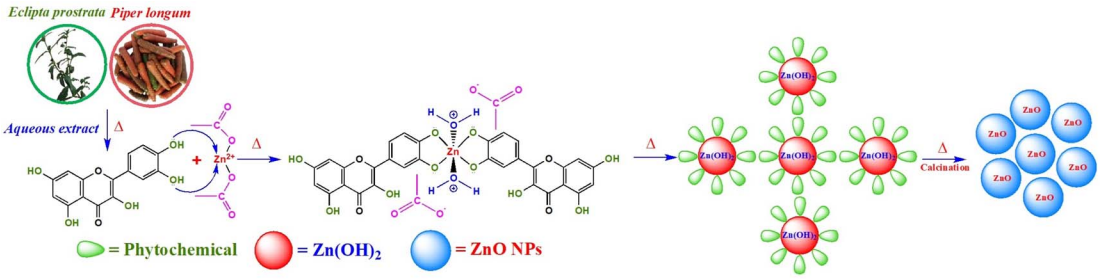

Fig. 2 Plausible mechanism for green synthesis of ZnONPs using quercetin as one of the phytochemicals in the aqueous extract of *E. prostrata* leaves and *P. longum* fruits.

63.17°, 66.70°, 68.26°, 69.38°, 72.87°, and 77.26°. Furthermore, diffraction peaks of ZnO_EPE at pH 10 displayed 2θ values of 32.04°, 34.70°, 36.52°, 47.81°, 56.85°, 63.12°, 66.68°, 68.21°, 69.32°, 72.79°, and 77.21°. These 2θ values aligned with diffraction planes (100), (002), (101), (102), (110), (103), (200), (112), (201), (004), and (202), respectively, matching with the hexagonal wurtzite structure of ZnONPs (JCPDS no. 36-1451).[38] Importantly, the XRD pattern of ZnO_EPE showed no impurity peaks, affirming the pure nature of ZnO_EPE.

The average particle sizes of ZnO_EPE nanoparticles at pH 7, pH 8, pH 9, and pH 10, determined based on the most intense diffraction peak at $2\theta = 36°$ (101) using the Debye–Scherrer equation, were 17.30 nm, 17.62 nm, 20.73 nm and 18.09 nm, respectively. Similar observations were noted in ZnO_PLE. The XRD pattern of ZnO_PLE at different pH values showed diffraction peaks located around 32° (100), 34° (002), 36° (101), 47° (102), 56° (110), 63° (103), 66° (200), 68° (112), 69° (201), 72° (004), and 77° (202), indicating that ZnO_PLE nanoparticles exhibit a fine hexagonal crystalline structure. The absence of diffraction peaks rather than peaks of ZnONPs suggests that the ZnONPs were uncontaminated by additional phase impurities, underscoring their elevated phase purity. The average crystallite sizes of ZnO_PLE nanoparticles at pH 7, pH 8, pH 9, and pH 10 were found to be 26.23 nm, 27.74 nm, 29.47 nm, and 27.77 nm, respectively. The outcomes showed that crystallite sizes of ZnO_EPE as well as ZnO_PLE gradually increased with increase in pH, and a slight decrease occurred at higher pH owing to the dissolution of ZnONPs, leading to smaller particle sizes and agglomeration.[39]

The impact of Zn^{2+} concentrations on the particle size of both ZnO_EPE and ZnO_PLE was determined at different concentrations (0.05–0.2 M). The XRD pattern of all samples in Fig. 4 shows the peaks at 32°, 34°, 36°, 47°, 56°, 63°, 66°, 68°, 69°, 72°, and 77°, which correspond to the hexagonal crystalline structure of ZnONPs. The average crystallite sizes of ZnO_EPE at Zn^{2+} concentrations of 0.05 M, 0.10 M, 0.15 M, and 0.20 M were

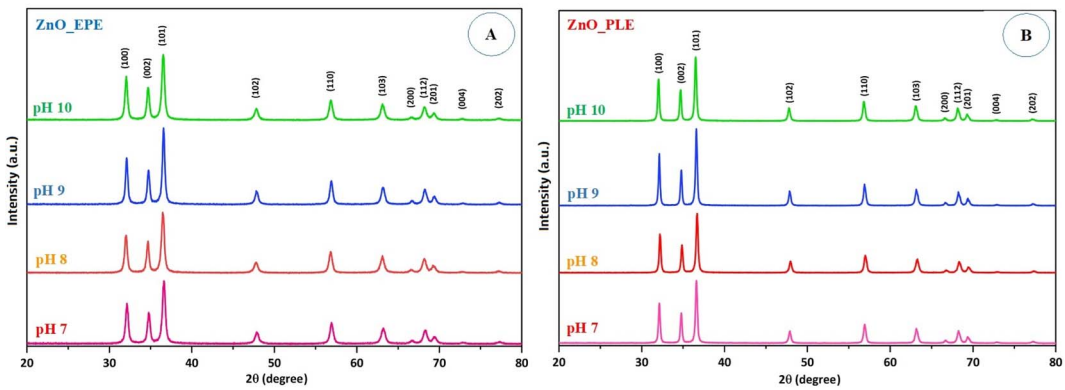

Fig. 3 XRD pattern of (A) ZnO_EPE and (B) ZnO_PLE synthesized at different pH values.

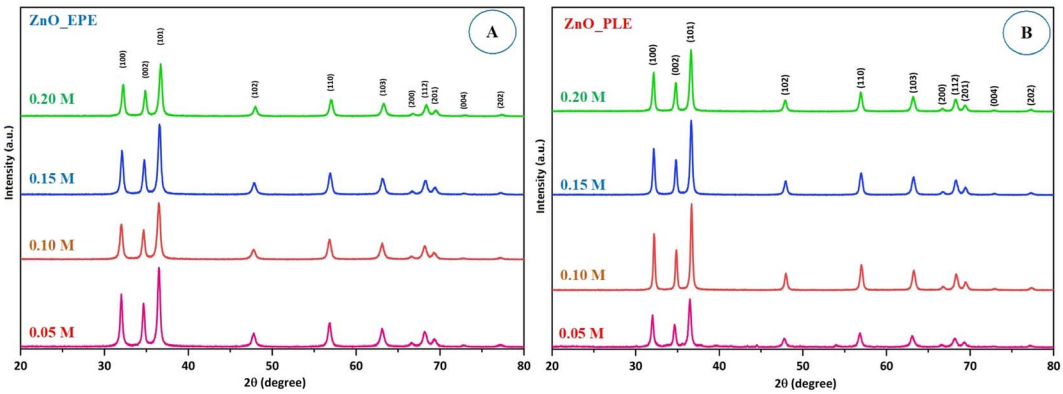

Fig. 4 XRD pattern of (A) ZnO_EPE and (B) ZnO_PLE synthesized at different Zn^{2+} concentrations.

calculated to be 20.32 nm, 17.67 nm, 18.55 nm and 18.97 nm, respectively. Similarly, the corresponding average crystallite sizes of ZnO_PLE were found to be 26.23 nm, 22.07 nm, 21.29 nm, and 23.27 nm. According to these results, a rise in $[Zn^{2+}]$ tended to lower the crystallite size of ZnONPs. This phenomenon could be explained by an increase in Zn^{2+} concentration up to an optimum level subsequently facilitating accelerated particle growth, yielding nanoparticles of smaller size. However, at higher $[Zn^{2+}]$, the ZnONP size slightly increased. At higher $[Zn^{2+}]$ in the reaction mixture, it is possible to observe the shortage of functional groups, enhancing aggregation of growing nanoparticles, giving rise to bigger size nanoparticles.[40] Kaningini *et al.*[41] reported that concentrations of zinc nitrate hexahydrate up to 1 g lead to the formation of a smaller crystallite size of ZnO nanoparticles, while the crystallite size increased at 5 g of zinc nitrate hexahydrate.

3.3. Surface chemistry

Surface chemistry analysis identifies chemical bonds present in both the plant extract and the synthesized ZnONPs. The spectra of the EPE extract and ZnO_EPE nanoparticles are shown in Fig. 5a and b. The FTIR spectrum of EPE (Fig. 5a) reveals bands at 3436 cm^{-1} referring to O–H stretching of phenolic compounds, at 2974 cm^{-1} for –CH stretching vibration, at 1643 cm^{-1} for C=C stretching of aromatic compounds such as flavonoids, at 1394 cm^{-1} for C–H bonds in aldehydes, at 1054 cm^{-1} for C–O ether stretch, and at 879 cm^{-1} for N–H amine stretch. These results are in good agreement with those reported by Maheswari *et al.*[42] The FTIR spectrum (Fig. 5b) of ZnO_EPE nanoparticles exhibited a characteristic band at around 460–490 cm^{-1} corresponding to the stretching vibrations of Zn–O.[43] A broad peak at 3515 cm^{-1} could be attributed to the –OH group and surface water of ZnO_EPE nanoparticles. Meanwhile, the spectra of the PLE extract and ZnO_PLE nanoparticles are shown in Fig. 5c and d. The peaks of PLE were observed at 3305 cm^{-1} (–OH stretching vibration), 2927 cm^{-1} (–CH stretching of aromatic compound), 1636 cm^{-1} (C=C), 1445 cm^{-1} (–OH bond of polyphenols), and 1038 cm^{-1} (C–O–C).[44] Similar to the FTIR spectrum of ZnO_EPE, a characteristic peak at around 460–490 cm^{-1} is present, assigned to Zn–O bonds of ZnO_PLE nanoparticles.[43]

3.4. Optical properties

The optical absorption behavior of biosynthesized ZnO_EPE and ZnO_PLE nanoparticles was assessed using UV-DRS profiles, as shown in Fig. 6A. The spectra revealed that the absorption band edges at 415 nm for ZnO_EPE and 407 nm for ZnO_PLE may be attributed to the electron transition from the valence band (VB) to the conduction band (CB), corroborating prior research findings.[45] To further analyze the optical

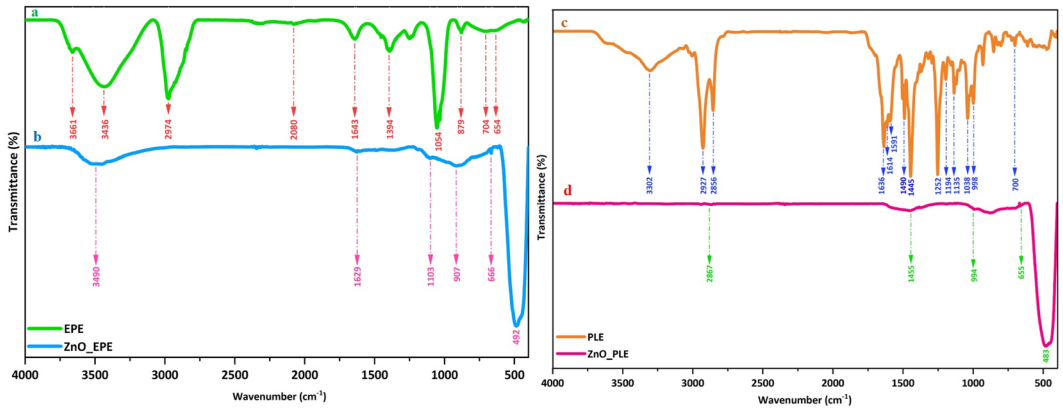

Fig. 5 FTIR spectra of (a) EPE, (b) ZnO_EPE, (c) PLE and (d) ZnO_PLE.

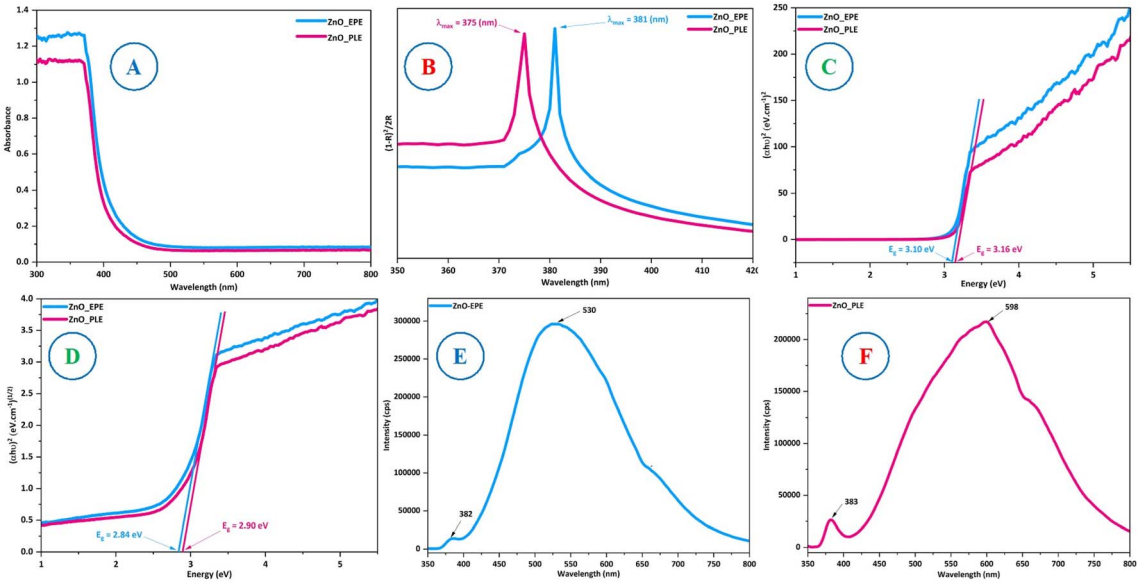

Fig. 6 (A) UV-Vis DRS profiles, (B) UV-Vis spectra, (C) direct bandgap values, (D) indirect bandgap values, and (E and F) photoluminescence spectra of ZnO_EPE and ZnO_PLE.

properties, the Kubelka–Munk function (eqn (2)) is employed to transform diffuse reflectance data into absorption coefficients (α). As illustrated in Fig. 6B, absorption bands at 381 nm and 375 nm are observed for ZnO_EPE and ZnO_PLE nanoparticles, consistent with existing literature.[46] The bandgap energy of ZnO_EPE and ZnO_PLE was measured using the Kubelka–Munk function (eqn (1)) and Tauc's equation (eqn (2)), as follows:

$$F(RE) = (1 - RE)^2/(2 \times RE) \quad (1)$$

$$(F(R)h\nu)^n = B(E - E_g) \quad (2)$$

where R, E, h, B, ν, n and E_g represent the reflectance coefficient, photon energy, Planck constant, a constant coefficient, frequency, the type of optical transition of the semiconductor (for indirect transition $n = 1/2$ and for direct transition $n = 2$) and bandgap energy, respectively. Direct bandgap values are determined to be 3.10 eV for ZnO_EPE and 3.16 eV for ZnO_PLE, corresponding to indirect bandgap values of 2.84 eV and 2.90 eV, as depicted in Fig. 6C and D. The findings reveal subtle discrepancies in bandgap energies attributed to the difference in plant extracts utilized in the ZnONP production. This observation aligns with established literature on green-synthesized ZnO nanoparticles and direct bandgap energies of both biosynthesized ZnO nanoparticles.[47]

The photoluminescence (PL) spectra of ZnO_EPE and ZnO_PLE at an excitation wavelength of 325 nm are shown in Fig. 6E and F. Both types of biosynthesized ZnO exhibit distinct peaks. The PL spectra of ZnO_EPE nanoparticles showed a UV emission peak at 382 nm and a broad-deep level visible emission peak at 530 nm. Similarly, the PL spectra of ZnO_PLE nanoparticles revealed peaks around 383 nm and 598 nm. The initial peaks at approximately 382 nm or 383 nm denote UV arising from the band edge of the ZnO_EPE or ZnO_PLE nanoparticles, indicating the recombination of free excitons through an exciton–exciton collision process.[48] The calculated bandgaps for these emissions, 3.25 eV and 3.24 eV respectively, align closely with the Tauc plot band gap, as depicted in Fig. 6C. Furthermore, the second broad-deep level emission peaks of ZnO_EPE at 530 nm and ZnO_PLE at 538 nm are attributed to the radiative recombination of holes in the VB and electrons in the CB, associated with singly ionized oxygen vacancies.[49] These findings corroborate existing literature on ZnO nanoparticle photoluminescence behavior.[50]

3.5. Zeta potential and BET surface analysis

Zeta potential measurement provides information about surface charges present on ZnO nanoparticles, thus contributing to a deeper understanding of their potential stability in colloidal suspension. Furthermore, zeta potential can provide valuable insights into the particle distribution and aggregation behavior. Nanoparticles with large negative or positive zeta potential values experience no aggregation due to electrostatic repulsion among the particles, leading to an increase in the stability of the formulation.[51] Meanwhile, particles with low zeta potential values tend to aggregate due to interparticle van der Waals attractions. Typically, zeta potential values higher than +30 mV or lower than −30 mV are considered indicative of good nanoparticle stability.[52] The zeta potential values of the biosynthesized ZnONPs, as shown in Fig. 7, were found to be −42.2 mV for ZnO_EPE and −62.6 mV for ZnO_PLE, confirming the stability of the synthesized ZnO nanoparticles.

The antibacterial, antioxidant, and photocatalytic activities of ZnONPs are widely recognized to be influenced by their specific surface area (S_{BET}). Through BET analysis, S_{BET} values of ZnO_EPE and ZnO_PLE NPs were measured to be relatively low,

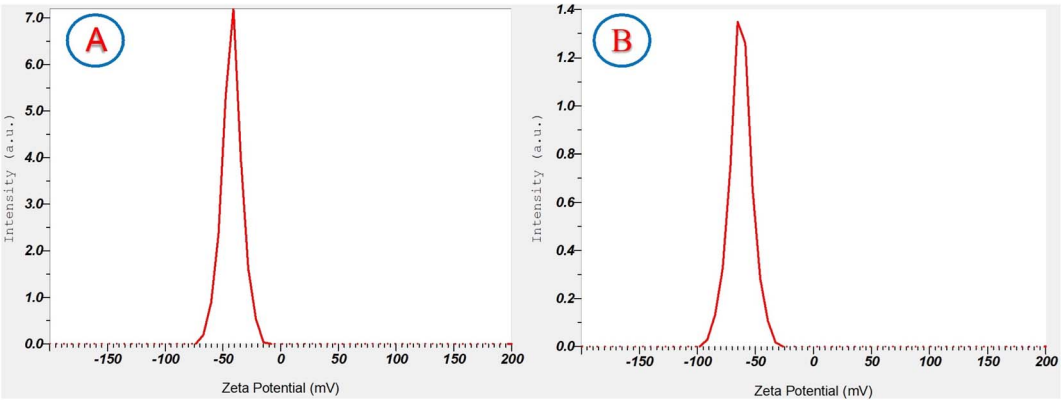

Fig. 7 Zeta potential of (A) ZnO_EPE and (B) ZnO_PLE nanoparticles.

at around 8.6 $m^2 g^{-1}$ and 8.0 $m^2 g^{-1}$, respectively. The results indicate that ZnO_EPE NPs possess a slightly larger surface area with a greater abundance of active sites compared to ZnO_PLE NPs. Similarly, several studies also reported low surface areas of ZnONPs biosynthesized using the *Pontederia crassipes* leaf extract ($S_{BET,ZnO}$: 12.8 $m^2 g^{-1}$),[53] *Zea mays* husk extract ($S_{BET,ZnO}$: 11.3 $m^2 g^{-1}$),[54] and *Artocarpus heterophyllus* peel extract ($S_{BET,ZnO}$: 6.6 $m^2 g^{-1}$).[54] This distinction suggests that ZnO_EPE NPs may exhibit enhanced bioactive applications and photocatalytic processes relative to ZnO_PLE NPs.

3.6. Morphology and composition

The morphology and size of green synthesized ZnO_EPE and ZnO_PLE nanoparticles were examined using SEM as shown in Fig. 8A and B. The outcomes reveal that the morphology of ZnO_EPE was uneven, with heterogeneous particles exhibiting quasi-spherical and rod-like shapes with aggregations. This irregular shape is common in metal oxides formed during solution combustion processes.[55] The particles of ZnO_PLE show spherical shapes with little agglomeration, as represented in Fig. 8C and D. This agglomeration observed in SEM images can be attributed to high polarity and electrostatic attraction between ZnONPs.[56] The sizes of ZnO_EPE and ZnO_PLE were determined to be 16–58 nm and 27–78 nm, respectively. The morphology and size of the ZnO_EPE and ZnO_PLE are also shown in TEM micrographs (Fig. 9). Fig. 9A and B display the TEM images of the spherical shaped ZnO_EPE in selected areas where the uniform spheres have particles size from 14 nm to 58 nm. The TEM images of ZnO_PLE shown in Fig. 9C and D show that the shape of the nanoparticles is spherical and their size ranges from 16 nm to 97 nm. These results are in accordance with the SEM observations (Fig. 8) and are higher than

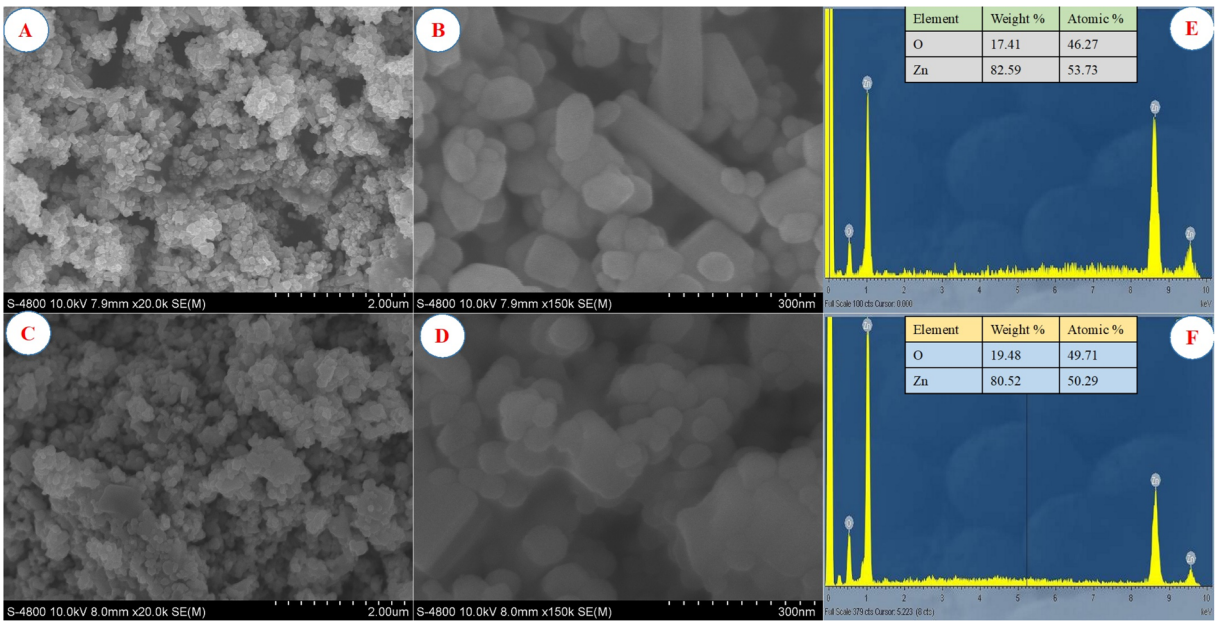

Fig. 8 Low and high magnification SEM images of (A and B) ZnO_EPE and (C and D) ZnO_PLE; EDX spectra and elemental composition (table inset) of (E) ZnO_EPE and (F) ZnO_PLE.

their crystal sizes calculated from XRD profiles owing to the polycrystalline aggregation.[57] Recent research on the green synthesis of ZnONPs, along with various morphologies and sizes, is listed in Table 3. EDX measurements were carried out to determine the elemental composition of the ZnO_EPE and ZnO_PLE, with the results presented in Fig. 8E and F. The EDX spectrum of both ZnO samples showed only the presence of zinc (Zn) and oxygen (O) without any other compositions, indicating the formation of biosynthesized ZnO nanoparticles in a pure chemical state. The quantitative analysis of all elemental constituents of ZnO_EPE and ZnO_PLE is summarized in the table inserted in Fig. 8E and F. The compositions of obtained peaks were Zn (53.73%) and O (46.27%) for ZnO_EPE while the chemical composition of ZnO_PLE exhibited Zn (50.29%) and O (49.71%). These results closely align with the findings of the chemical composition [Zn (43.07%) and O (56.93%)] of ZnONPs synthesized using the *R. tuberosa* extract as reported by Vasantharaj *et al.*[58]

3.7. Photocatalytic performance of green ZnONPs

The investigation into the photocatalytic performance of ZnONPs biosynthesized utilizing extracts from the *E. prostrata* or *P. longum* was conducted by evaluating the degradation

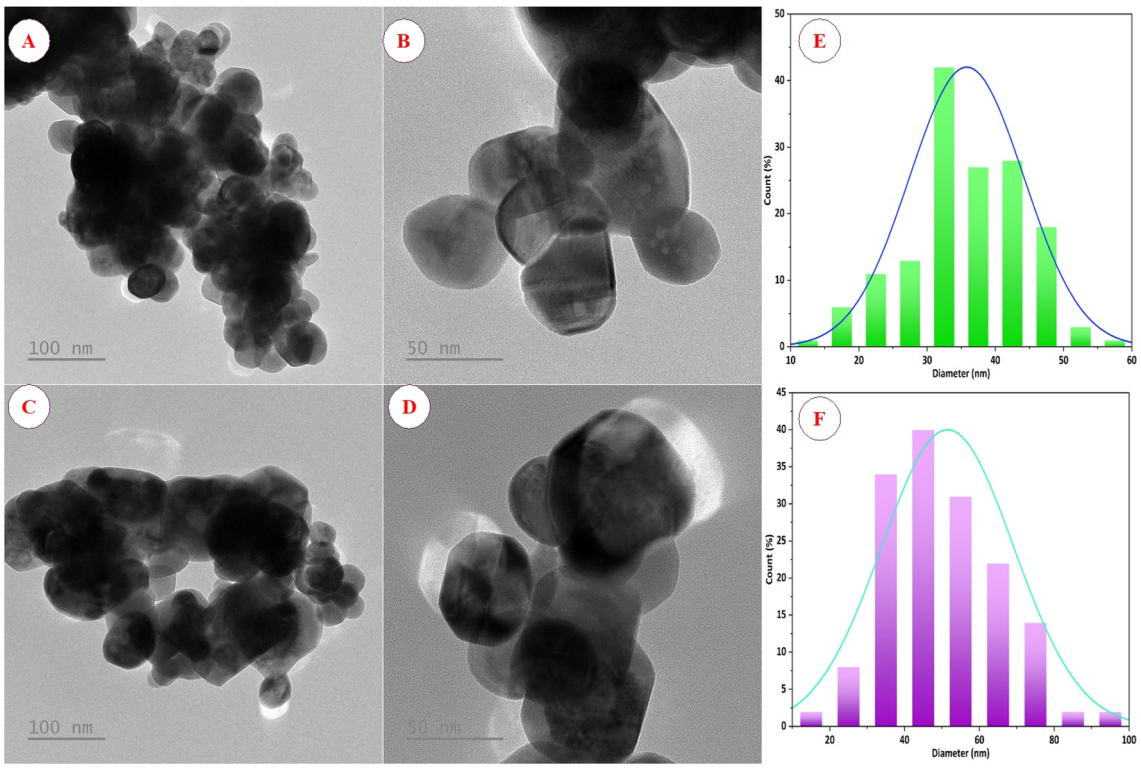

Fig. 9 TEM images (C and D) at low and high magnifications and size distribution histograms of ZnO_EPE (A, B and E) and ZnO_PLE (C, D and F).

Table 3 Comparison of properties and applications of green ZnONPs synthesized using different plant extracts

Zn source	Plant source	Particle size	Morphology	Application	Reference
Zinc acetate	*A. esculentus* mucilage	20–70 nm	Spherical and rod shape	Photocatalytic degradation	59
Zinc acetate	*M. fragrans* fruit	41.23 nm	Spherical or elliptical shape	Photocatalytic degradation, antibacterial, antidiabetic, antiparasitic, larvicidal and antioxidant activity	60
Zinc acetate	*A. barbadensis* Mill. leaf	35 nm	Spherical shape	Seeding growth and germination	61
Zinc nitrate	*P. hysterophorus* L. leaf	27–84 nm	Spherical and hexagonal shape	Antifungal activity	62
Zinc nitrate	*Zea mays* husk, *A. heterophyllus* peel, *P. granatum* peel	28–74 nm	Flower shape	Antibacterial and antioxidant activity	54
Zinc acetate	*E. prostrata* leaves	14–58 nm	Spherical and rod shape	Photocatalytic degradation, antibacterial and antioxidant activity	Present work
Zinc acetate	*P. longum* fruits	16–97 nm	Spherical shape	Photocatalytic degradation, antibacterial and antioxidant activity	Present work

efficiency under direct solar light irradiation. Fig. 10 shows that both ZnO_EPE and ZnO_PLE exhibited poor CV dye adsorption percentages at approximately 6.11% and 6.40%, respectively, after 60 min of stirring in darkness. Adsorption works out thanks to the electrostatic attraction between the negative charges of ZnONPs and the positive charges of CV dye. The results from the photocatalytic degradation of CV under solar light for both ZnO_EPE and ZnO_PLE suggest significantly high photocatalytic activity. In particular, ZnO_PLE nanoparticles demonstrated superior degradation, achieving a remarkable 99.90% degradation at 120 min, while ZnO_EPE nanoparticles attained a slightly lower degradation of 95.64%. This difference is elucidated by the substantial amount of CV adsorbed on the ZnO_PLE surface, coupled with dispersion and size distribution of ZnONPs, contributing to enhanced photocatalytic efficiency. Indeed, the photocatalytic performance of ZnONPs depends on their morphology, size, and crystallographic structure.[63] The solar light-induced CV degradation kinetics catalyzed by ZnO_EPE or ZnO_PLE could be assessed using the Langmuir–Hinshelwood equation (eqn (3)).

$$\ln\frac{C_o}{C_t} = kt \tag{3}$$

where C_o: CV concentration at $t = 0$ min, C_t: CV concentration at any time t, and k: rate constant of the pseudo first-order reaction. Fig. 10E demonstrates that the rate constant (k) of ZnO_PLE is 0.0593 min^{-1}, which is higher than that of ZnO_EPE (0.0273 min^{-1}), indicating that ZnO_PLE exhibits better photoreactivity towards CV dye than ZnO_EPE.[3] Comparative results of the photocatalytic performance of various NPs are listed in Table 4, indicating higher activities of both ZnO_PLE and ZnO_EPE.

The photocatalysis mechanism, as illustrated in Fig. 11, was proposed to further understand the role of ZnO_EPE or ZnO_PLE in degradation of CV. First, under solar irradiation, ZnO nanoparticles were subjected to energy equal to or greater than bandgap energies (in this case, 3.16 eV for ZnO_EPE and 3.10 eV for ZnO_PLE). This led to the excitation of electrons from the VB to CB, generating electron–hole pairs that migrated to the surface of ZnONPs. Subsequently, holes in the valence band

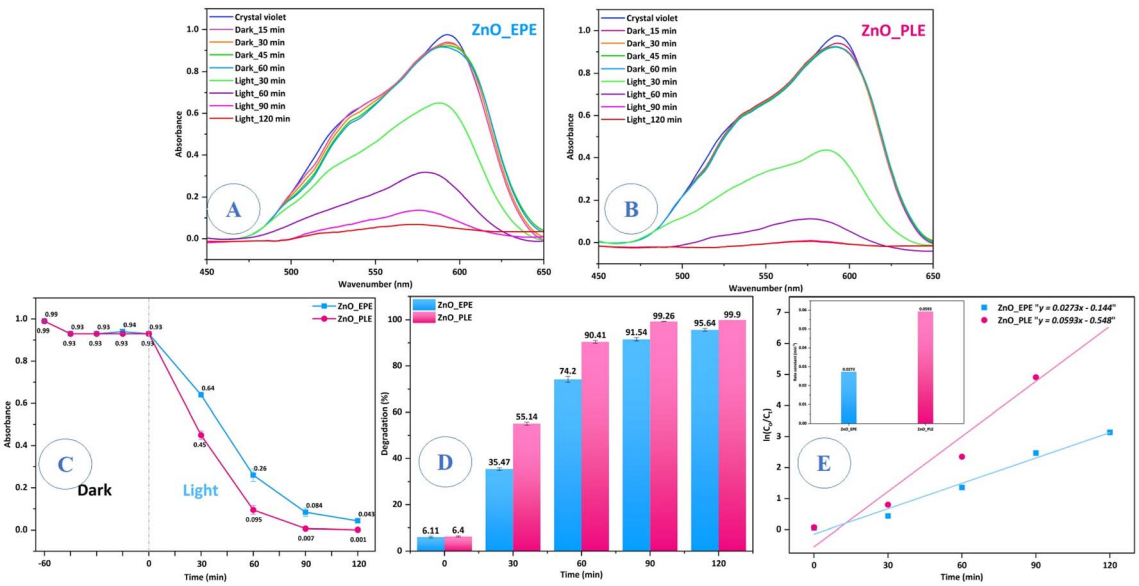

Fig. 10 Photocatalytic activity of ZnO_EPE and ZnO_PLE: (A–C) absorption spectra of CV dye *versus* irradiation time, (D) photocatalytic degradation *versus* irradiation time, (E) pseudo-first order kinetics for CV degradation *versus* irradiation time.

Table 4 Comparison of photocatalytic performance of biosynthesized NPs for degradation of dyes

Nanomaterial	Synthesis method	Light source	Target	Degradation time	Reference
In_2O_3 NPs	Green synthesis	W-lamp light	Crystal violet	93.7% in 80 min	64
Cu–Ni NPs	Green synthesis	UV light	Crystal violet	95.6% in 160 min	65
CuO NPs	Green synthesis	Sunlight	Crystal violet	87.0% in 100 min	66
ZnONPs	Co-precipitation	UV light	Crystal violet	82.0% in 240 min	67
ZnONPs	Green synthesis	UV light	Crystal violet	76.0% in 90 min	68
			Methylene blue	81.5% in 120 min	
			Phenol red	83.0% in 90 min	
ZnO_EPE NPs	Green synthesis	Sunlight	Crystal violet	95.6% in 120 min	Present work
ZnO_PLE NPs	Green synthesis	Sunlight	Crystal violet	99.9% in 120 min	Present work

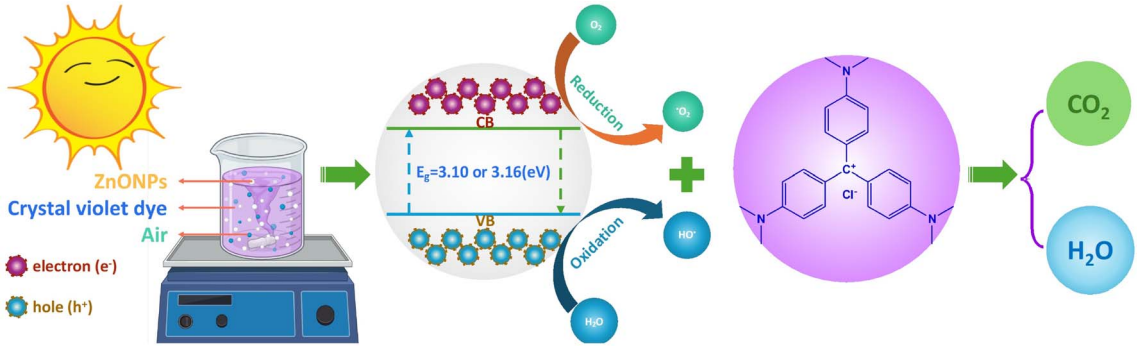

Fig. 11 Plausible mechanism for photodegradation of CV dye of ZnO_EPE and ZnO_PLE.

directly oxidized with H_2O or OH^-, yielding hydroxyl radicals ($^{\bullet}OH$), while the photogenerated electrons in the conduction band reduced O_2, giving rise to superoxide anion radicals ($O_2^{\bullet-}$). Ultimately, $O_2^{\bullet-}$ and $^{\bullet}OH$ radicals played a crucial role in degrading crystal violet in the water-based solution, yielding environmentally friendly and non-toxic byproducts such as CO_2 and H_2O as shown in the equations below:

$$ZnONPs + h\nu \rightarrow ZnONPs\ (h^+, VB) + ZnONPs\ (e^-, CB)$$

$$ZnONPs\ (e^-, CB) + O_2 \rightarrow ZnONPs + O_2^{\bullet-}$$

$$ZnONPs\ (h^+) + H_2O \text{ or } OH^- \rightarrow ZnONPs + OH^{\bullet} + H^+$$

$$O_2^{\bullet-} + H^+ \rightarrow {}^{\bullet}OOH$$

$$ZnONPs\ (h^+) + CV \rightarrow ZnONPs + CV^+$$

$$CV^+ + O_2^{\bullet-} + {}^{\bullet}OOH \rightarrow CO_2 + H_2O$$

To investigate the role of radicals in decomposition of crystal violet dye, runs were conducted the same as standard experiments and addition of 0.5 mM *tert*-butanol (*t*-BuOH), *p*-benzoquinone (BQ), and triethanolamine (TEOA) as scavengers for the hydroxyl radical ($OH^{\bullet}$), superoxide radical ($O_2^{\bullet-}$), and holes (h^+), respectively. As depicted in Fig. 12, the photocatalytic efficiency of ZnO_EPE and ZnO_PLE decreased when *p*-benzoquinone was added as a superoxide radical scavenger, dropping from 94.87% to 57.85% and from 99.52% to 70.53%, respectively, compared to conditions without a scavenger. Similarly, in the presence of triethanolamine as a hole scavenger, the degradation rate of CV was 72.65% (for ZnO_EPE) and 76.61% (for ZnO_PLE). However, *tert*-butanol had no significant effect on CV dye degradation, indicating that $OH^{\bullet}$ had a lesser impact on the photocatalytic reaction. These results indicate that the role of holes and electrons were not identical, suggesting that $O_2^{\bullet-}$ was generated by the reaction between CB electrons and O_2. Since the CV dye degradation was affected by addition of triethanolamine, the direct impact of photogenerated holes on the dye degradation process should also be considered. Consequently, the photocatalytic reaction mechanism involves pivotal species, which can be specified as $O_2^{\bullet-}$, h^+, and $OH^{\bullet}$.

3.8. Bioactive applications

3.8.1. Antibacterial activity. Antibacterial activity of ZnO_EPE and ZnO_PLE was investigated against Gram-negative bacteria (*E. coli* and *S. typhimurium*) and Gram-positive bacteria (*S. aureus* and *B. cereus*), as shown in Fig. 13. According to Table 5, both types of ZnONPs in this study exhibited good antibacterial activity. ZnO_EPE NPs demonstrated potent antibacterial

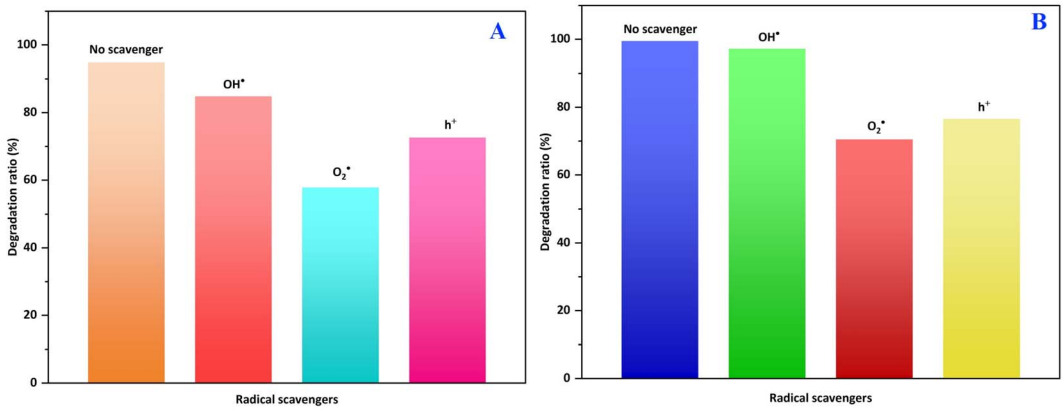

Fig. 12 The photocatalytic activity of (A) ZnO_EPE and (B) ZnO_PLE in the presence of *t*-BuOH, TEOA, and BQ for the degradation of CV dye.

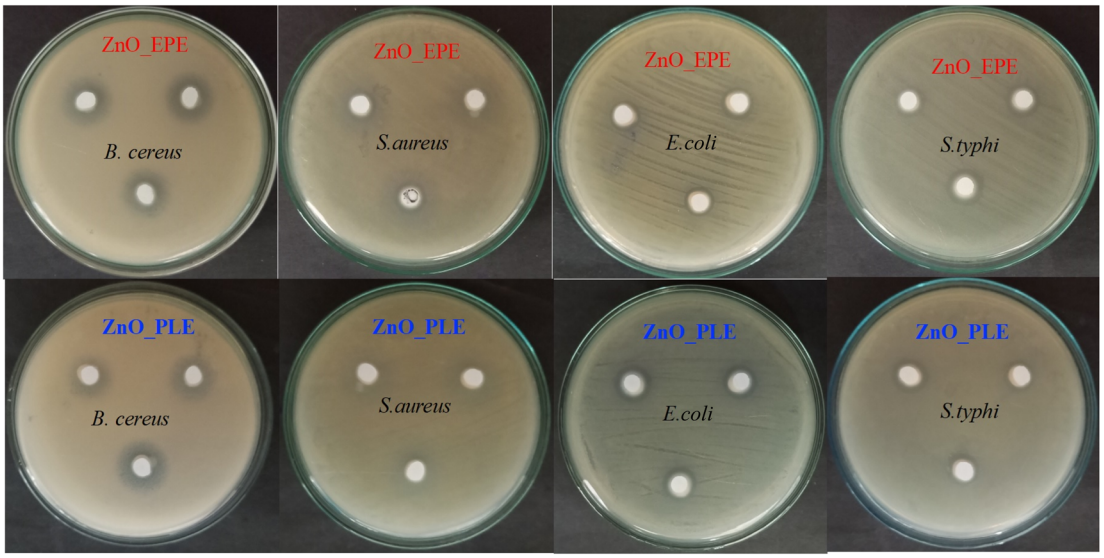

Fig. 13 Antibacterial activity of ZnO_EPE and ZnO_PLE nanoparticles against *E. coli*, *S. aureus*, *B. cereus* and *S. typhi*.

Table 5 Antibacterial assay of synthesized ZnO nanoparticles against the test bacteria

	Zone of inhibition (mm)	
Bacterial species	ZnO_EPE	ZnO_PLE
S. aureus	18.5 ± 0.1	13.4 ± 0.3
B. cereus	13.6 ± 0.3	11.9 ± 0.3
E. coli	9.6 ± 0.3	9.9 ± 0.6
S. typhimurium	10.1 ± 0.3	10.1 ± 0.1

activity against *S. aureus* and *B. cereus*, with inhibition zones measuring 18.5 ± 0.1 mm and 13.6 ± 0.3 mm, respectively, which were higher compared to ZnO_PLE NPs, which exhibited inhibition zones of 13.4 ± 0.3 mm for *S. aureus* and 11.9 ± 0.3 mm for *B. cereus*. However, the inhibition zones of ZnO_EPE NPs against *E. coli* (9.6 ± 0.3 mm) and *S. typhimurium* (10.1 ± 0.3 mm) were similar to those of ZnO_PLE NPs (9.9 ± 0.6 mm against *E. coli* and 10.1 ± 0.1 mm). This discrepancy in activity can be attributed to variation in the surface area between ZnO_EPE (8.582 m^2 g^{-1}) and ZnO_PLE (7.998 m^2 g^{-1}), with a larger surface area facilitating enhanced interaction with bacteria, thereby augmenting antimicrobial activity.[69]

The minimum inhibitory concentration (MIC) data were obtained using the broth dilution method for both *S. aureus* and *E. coli* bacterial strains to determine the minimum quantity of ZnONPs needed to inhibit microbial growth. As depicted in Fig. 14, ZnO_EPE NPs exhibit MIC values of 62.5 μg mL^{-1} and 31.2 μg mL^{-1} against *E. coli* and *S. aureus* bacteria, respectively. Compared to ZnO_PLE NPs, the MIC values of ZnO_EPE NPs were similar, indicating their potent antibacterial properties. The results suggest that both ZnO_EPE and ZnO_PLE NPs are bacteriostatic at low concentrations. Previous reports also revealed that the MIC values of ZnONPs biosynthesized using the *A. altissima* leaf extract against *E. coli*, *K. pneumoniae*, *S. aureus* and *S. pyogenes* were 0.3125 mg mL^{-1}, 0.625 mg mL^{-1}, 0.3125 mg mL^{-1} and 0.625 mg mL^{-1}, respectively.[70]

As a result, both ZnO_EPE and ZnO_PLE NPs may be more effective against Gram-(+) bacteria than against Gram-(−) bacteria. This finding aligns with antibacterial activity of ZnONPs synthesized using the *A. marmelos* leaf extract, which was greater against Gram-(+) (*S. aureus*) than Gram-(−) (*K.*

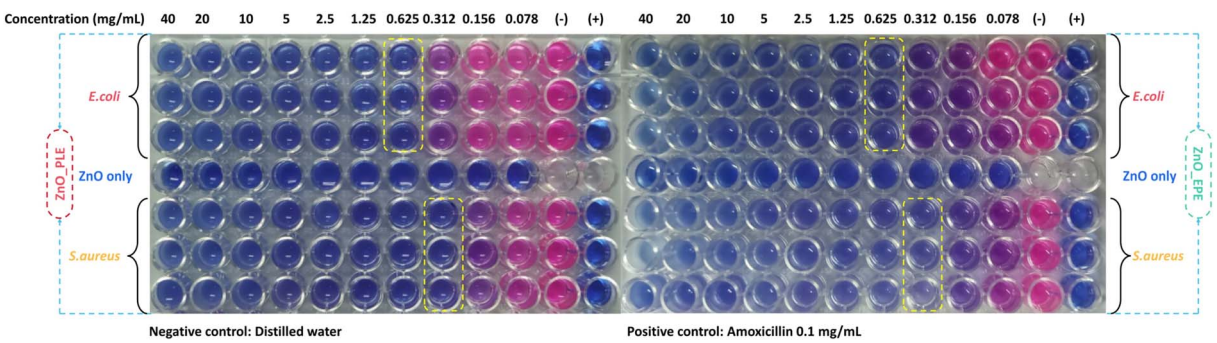

Fig. 14 MIC values of ZnO_EPE and ZnO_PLE NPs against *E. coli* and *S. aureus* bacteria.

pneumonia) bacteria as reported by Dhiman *et al.*[71] In another study, Şahin *et al.*[72] utilized the aqueous leaf extract of *T. syriacus* to synthesize ZnONPs. These authors observed a stronger antibacterial activity against Gram-(+) bacteria such as *C. michiganensis* and *B. subtilis*, compared to Gram-(−) bacteria including *P. syringae*, *P. cichorii*, *X. axonopodis* and *P. carotovorum*. Similarly, Sama *et al.*[73] also reported that ZnONPs biosynthesized using the *C. album* L. leaf extract had less antimicrobial activity against Gram-(−) bacteria than against Gram-(+) bacteria. Their investigations highlighted a greater resistance of Gram-negative *E. coli* to ZnO nanocrystals compared to Gram-positive *S. aureus*.

The mentioned phenomenon underscores the importance of considering the differing cell wall structures of Gram-(+) and Gram-(−) bacteria in contact with ZnONPs. Gram-(+) bacteria possess a thick cell wall with multilayers of peptidoglycan. By contrast, Gram-(−) bacteria have a thinner cell wall with a peptidoglycan layer.[74] The ZnO nanoparticles attach directly to the outer cell wall of Gram-(+) bacteria, which consists of plenty of pores facilitating nanoparticle penetration, resulting in intracellular content leakage, causing cell death without cell breakage (Fig. 15). On the other hand, ZnO nanoparticles interact directly with the outer cell wall of Gram-(−) bacteria, which contains lipoprotein, phospholipids, and lipopolysaccharide, acting as a barrier against ZnO nanoparticles penetration.[75] In contrast, a previous study reported that the antibacterial activity of synthesized ZnONPs from date pulp waste was more efficient against Gram-(−) than Gram-(+) bacterial pathogens.[76] Additionally, Aldeen *et al.*[3] investigated the antibacterial activity of ZnONPs synthesized from *P. roebelenii* leaves against *S. aureus*, *S. pneumoniae*, *E. coli* and *S. typhi* bacteria. The results revealed that the biosynthesized ZnONPs exhibited the most significant effect against Gram-(−) bacteria compared to Gram-(+) bacteria. ZnONPs have various mechanisms for causing antibacterial action, the most common of which is the interaction between nanoparticles and bacteria, the release of Zn^{2+} ion, penetration through the cell membrane, and the generation of reactive oxygen species to destroy lipids, protein and bacterial DNA, ultimately leading to bacteria death (Fig. 15).[77]

3.8.2. Antioxidant activity. Antioxidant assays were conducted on ZnO_EPE and ZnO_PLE nanoparticles using DPPH and ABTS free radical scavenging assays, commonly utilized to evaluate the radical scavenging activity of nanoparticles. When the concentration of both biosynthesized ZnO increased from 250 μg mL^{-1} to 2500 μg mL^{-1}, the percentage inhibition also increased (Fig. 16). At 2500 μg mL^{-1}, ZnO_EPE exhibited a maximum DPPH free radical inhibition of 80.83%, while ZnO_PLE showed 83.37% inhibition. Similarly, for ABTS free radicals, ZnO_EPE and ZnO_PLE demonstrated inhibition rates of 99.30% and 99.67%, respectively. Here, both ZnO_EPE and ZnO_PLE NPs exhibited stronger inhibition of the ABTS radical compared to the DPPH radical. This finding may be attributed to the heightened sensitivity of ABTS, as it displays faster reaction kinetics, thereby generating a more pronounced response to antioxidants.[78] In Table 6, the percentages of DPPH and ABTS free radicals scavenged by gallic acid, a well-known standard antioxidant, were compared to those scavenged by ZnO_EPE and ZnO_PLE nanoparticles as well as EPE and PLE extracts. The biosynthesized ZnONPs and plant extracts displayed a moderate scavenging capability compared to the standard gallic acid. Notably, the comparison investigation

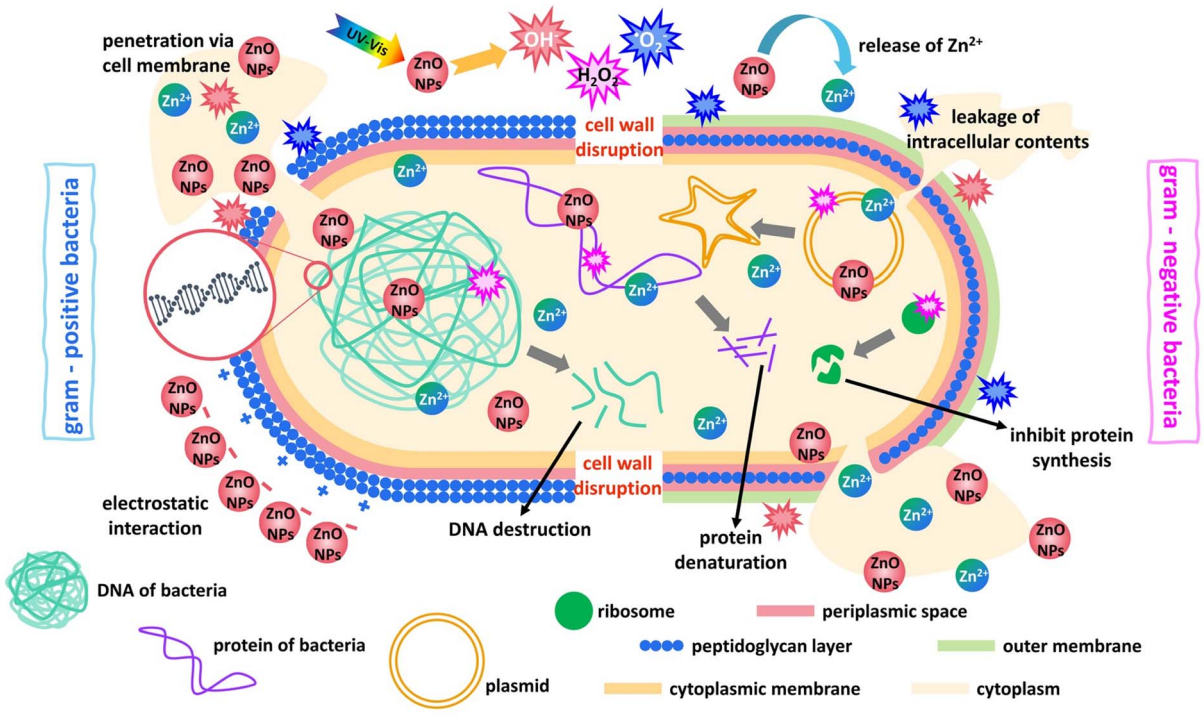

Fig. 15 Proposed mechanism of antibacterial activity of ZnONPs.

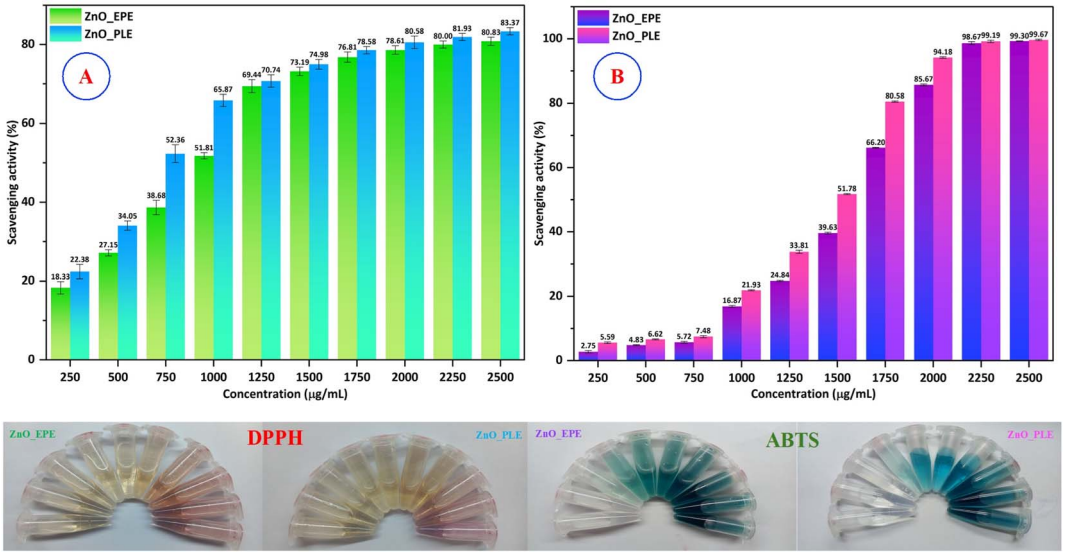

Fig. 16 (A) DPPH and (B) ABTS scavenging studies of ZnO_EPE and ZnO_PLE nanoparticles.

Table 6 Antioxidant activity of ZnO nanoparticles

	IC_{50} (μg mL^{-1})	
Samples	DPPH	ABTS
ZnO_EPE	925.69 ± 24.10	1546.90 ± 2.53
ZnO_PLE	767.84 ± 13.85	1415.62 ± 1.77
EPE	1270.03 ± 9.80	2049.64 ± 4.25
PLE	1891.87 ± 10.90	2433.60 ± 6.85
GA	1.30 ± 0.01	10.19 ± 0.01

revealed that ZnO_PLE showed an antioxidant capacity on par with that of ZnO_EPE NPs. In the ABTS assay, the IC_{50} values of ZnO_EPE and ZnO_PLE were 1533.32 μg mL^{-1} and 1390.80 μg mL^{-1}, respectively, whereas for DPPH assay, the IC_{50} values were observed as 925.70 μg mL^{-1} and 767.88 μg mL^{-1}, respectively. Therefore, the results indicate that both ZnO_EPE and ZnO_PLE nanoparticles possess promising antioxidant properties.

4 Conclusion

Here, ZnONPs were successfully synthesized through a green method using *E. prostrata* leaves and *P. longum* fruits as reducing and capping agents. Comprehensive characterization of the biosynthesized ZnONPs was performed, encompassing structural, morphological, optical and elemental analyses conducted *via* FTIR, SEM, TEM, XRD, DRS and EDX. The ZnO_EPE exhibited quasi-spherical and rod-like shapes ranging from 16–58 nm, while the ZnO_PLE showcased spherical morphology with an average diameter of 27–78 nm. FTIR analysis confirmed the presence of Zn–O bond peaks within the range of 460–490 cm^{-1}. Zeta potential measurements demonstrated negative values (−42.2 mV for ZnO_EPE and −62.6 mV for ZnO_PLE), indicating enhanced stability. In terms of CV dye degradation under natural sunlight, ZnO_PLE exhibited superior catalytic activity (99.90%) compared to ZnO_EPE (95.64%). Furthermore, ZnO_PLE and ZnO_EPE pseudo-first order kinetics were calculated to be 0.0593 min^{-1} and 0.0273 min^{-1}, respectively. Principally, the superoxide radical ($O_2^{\bullet-}$) was responsible for the degradation of CV dye contaminants. In the biological studies, both ZnO_EPE and ZnO_PLE demonstrated pronounced antibacterial activity against Gram-(+) bacterial strains compared to Gram-(−) bacterial strains and exhibited antioxidant properties. Overall, the ZnONPs obtained in this study have a promising future in photocatalytic, antimicrobial and antioxidant applications.

Data availability

The data supporting this article have been included as part of the ESI.†

Author contributions

Tran Thanh Xuan: software, investigation. Bien Thi Lan Thanh: methodology, supervision. Thuan Van Tran: conceptualization, validation, writing – review & editing. Nguyen Thi Thanh Thuy: conceptualization, methodology, writing – original draft, supervision, project administration.

Conflicts of interest

The authors declare no conflict of interest.

Acknowledgements

This research was funded by the Ministry of Education and Training (MOET), Vietnam under Grant Code: B2024-NLS-02. The authors sincerely thank the Ministry of Education and Training and Nong Lam University Ho Chi Minh City supported the implementation of this study.

References

1 S. Kumar, N. Bithel, S. Kumar, Kishan, M. Sen and C. Banerjee, *S. Afr. J. Bot.*, 2024, **164**, 146–151.
2 A. Dey, *Mater. Sci. Eng., B*, 2018, **229**, 206–217.
3 T. S. Aldeen, H. E. Ahmed Mohamed and M. Maaza, *J. Phys. Chem. Solids*, 2022, **160**, 110313.
4 M. Gadewar, G. K. Prashanth, M. Ravindra Babu, M. S. Dileep, P. Prashanth, S. Rao, M. Mahadevaswamy, M. Kumar Ghosh, N. Singh, S. K. Mandotra, A. Chauhan, S. Rustagi, R. Yogi, S. Chinnam, B. Ali, S. Ercisli and E. Orhan, *J. Saudi Chem. Soc.*, 2024, **28**, 101774.
5 M. Janani, T. Gomathi, R. Babujanarthanam and K. Kaviyarasu, *J. King Saud Univ., Sci.*, 2023, **35**, 102753.
6 N. Rani, S. Rani, H. Patel, Bhavna, S. Yadav, M. Saini, S. Rawat and K. Saini, *Inorg. Chem. Commun.*, 2023, **150**, 110516.
7 R. Sha, S. K. Puttapati, V. V. Srikanth and S. Badhulika, *J. Electroanal. Chem.*, 2017, **785**, 26–32.
8 Fahaduddin and T. Bal, *J. Mech. Behav. Biomed. Mater.*, 2024, **150**, 106330.
9 S. Thambidurai, P. Gowthaman, M. Venkatachalam and S. Suresh, *Optik*, 2020, **207**, 163865.
10 I. A. Ahmad and Y. H. Mohammed, *Micro Nanostruct.*, 2023, **181**, 207628.
11 S. B. Somvanshi, M. V. Khedkar, P. B. Kharat and K. M. Jadhav, *Ceram. Int.*, 2020, **46**, 8640–8650.
12 Z. Aalami, M. Hoseinzadeh, P. Hosseini Manesh, A. H. Aalami, Z. Es'haghi, M. Darroudi, A. Sahebkar and H. A. Hosseini, *Heliyon*, 2024, **10**, e24212.
13 S. Cui, Y. Wu, Z. Cui, P. He, N. Huang, W. Xu and J. Hu, *Mater. Lett.*, 2023, **341**, 134158.
14 S. Baskoutas, P. Giabouranis, S. N. Yannopoulos, V. Dracopoulos, L. Toth, A. Chrissanthopoulos and N. Bouropoulos, *Thin Solid Films*, 2007, **515**, 8461–8464.
15 J. Gaur, S. Kumar, M. Pal, H. Kaur, K. M. Batoo, J. O. Momoh and Supreet, *Hybrid Adv.*, 2024, **5**, 100128.
16 R. Perez-Cuapio, J. Alberto Alvarado, H. Juarez and H.-J. Sue, *Mater. Sci. Eng., B*, 2023, **289**, 116263.
17 C. M. Montemayor Palos, A. E. Mariño-Gámez, G.-E. Acosta-González, M. B. Hernández, S. García-Villarreal, L. Falcon Franco, L. García-Ortiz and J. A. Aguilar-Martínez, *Phys. B*, 2023, **656**, 414776.
18 G. Kalaiyan, S. Suresh, K. M. Prabu, S. Thambidurai, M. Kandasamy, N. Pugazhenthiran, S. K. Kumar and T. Muneeswaran, *J. Environ. Chem. Eng.*, 2021, **9**, 104847.
19 S. Venkatesan, S. Suresh, J. Arumugam, P. Ramu, N. Pugazhenthiran, R. Jothilakshmi and K. M. Prabu, *Results Chem.*, 2024, **7**, 101315.
20 O. J. Nava, C. A. Soto-Robles, C. M. Gómez-Gutiérrez, A. R. Vilchis-Nestor, A. Castro-Beltrán, A. Olivas and P. A. Luque, *J. Mol. Struct.*, 2017, **1147**, 1–6.
21 A. Kavitha, A. Doss, R. P. Praveen Pole, T. P. K. Pushpa Rani, R. Prasad and S. Satheesh, *Biocatal. Agric. Biotechnol.*, 2023, **48**, 102654.
22 S. Waseem, T. Sittar, Z. N. Kayani, S. S. A. Gillani, M. Rafique, M. Asif Nawaz, S. Masood Shaheen and M. A. Assiri, *Phys. B*, 2023, **663**, 415005.
23 M. Rafique, M. Sohaib, R. Tahir, M. B. Tahir, N. R. Khalid, M. Shakil, S. S. A. Gillani, M. I. Khan, H. Alrobei, K. Shahzad, A. M. Ali and S. Muhammad, *Optik*, 2021, **243**, 167495.
24 M. Sundrarajan, S. Ambika and K. Bharathi, *Adv. Powder Technol.*, 2015, **26**, 1294–1299.
25 S. Venkatesan, S. Suresh, P. Ramu, M. Kandasamy, J. Arumugam, S. Thambidurai, K. M. Prabu and N. Pugazhenthiran, *J. Indian Chem. Soc.*, 2022, **99**, 100436.
26 M. D. Jayappa, C. K. Ramaiah, M. A. P. Kumar, D. Suresh, A. Prabhu, R. P. Devasya and S. Sheikh, *Appl. Nanosci.*, 2020, **10**, 3057–3074.
27 L. Feng, Y.-Y. Zhai, J. Xu, W.-F. Yao, Y.-D. Cao, F.-F. Cheng, B.-H. Bao and L. Zhang, *J. Ethnopharmacol.*, 2019, **245**, 112109.
28 I.-M. Chung, G. Rajakumar, J.-H. Lee, S.-H. Kim and M. Thiruvengadam, *Appl. Microbiol. Biotechnol.*, 2017, **101**, 5247–5257.
29 Jyoti, S. P. S. Saini, H. Singh, S. S. Rath and N. K. Singh, *Exp. Parasitol.*, 2022, **241**, 108356.
30 B. R. Tiwari, M. Naseeruddin Inamdar, R. Orfali, A. Alshehri, A. Alghamdi, M. E. Almadani, S. Alshehri, S. Imam Rabbani and S. Mohammed Basheeruddin Asdaq, *Saudi Pharm. J.*, 2023, **31**, 101705.
31 S. Kumar, J. Kamboj, Suman and S. Sharma, *J. Acupunct. Meridian Stud.*, 2011, **4**, 134–140.
32 N. Viet Phong, D. Thi Nguyet Anh, H. Yeong Chae, S. Young Yang, M. Jeong Kwon, B. Sun Min and J. Ah Kim, *Bioorg. Chem.*, 2022, **128**, 106072.
33 D. Li, R. Wang, X. Cheng, J. Yang, Y. Yang, H. Qu, S. Li, S. Lin, D. Wei, Y. Bai and X. Zheng, *Nat. Prod. Res.*, 2022, **36**, 674–679.
34 P. A. Shenoy, S. S. Nipate, J. M. Sonpetkar, N. C. Salvi, A. B. Waghmare and P. D. Chaudhari, *J. Ethnopharmacol.*, 2013, **147**, 373–382.
35 T. T. T. Nguyen, Y. N. N. Nguyen, X. T. Tran, T. T. T. Nguyen and T. Van Tran, *J. Environ. Chem. Eng.*, 2023, **11**, 111003.
36 C. A. Soto-Robles, O. Nava, L. Cornejo, E. Lugo-Medina, A. R. Vilchis-Nestor, A. Castro-Beltrán and P. A. Luque, *J. Mol. Struct.*, 2021, **1225**, 129101.
37 C. M. Rafeeq, E. Paul, E. Vidya Saagar and P. P. Manzur Ali, *Ceram. Int.*, 2021, **47**, 12375–12380.
38 K. A. Sultana, M. T. Islam, J. A. Silva, R. S. Turley, J. A. Hernandez-Viezcas, J. L. Gardea-Torresdey and J. C. Noveron, *J. Mol. Liq.*, 2020, **307**, 112931.
39 S. S. Alias, A. B. Ismail and A. A. Mohamad, *J. Alloys Compd.*, 2010, **499**, 231–237.
40 H. M. H. Al-Kordy, S. A. Sabry and M. E. M. Mabrouk, *Sci. Rep.*, 2021, **11**, 10924.
41 A. G. Kaningini, S. Azizi, N. Sintwa, K. Mokalane, K. C. Mohale, F. N. Mudau and M. Maaza, *ACS Omega*, 2022, **7**, 31658–31666.

42 P. Maheswari, S. Harish, M. Navaneethan, C. Muthamizhchelvan, S. Ponnusamy and Y. Hayakawa, *Mater. Sci. Eng., C*, 2020, **108**, 110457.
43 H. Agarwal, A. Nakara, S. Menon and V. Shanmugam, *J. Drug Delivery Sci. Technol.*, 2019, **53**, 101212.
44 J. R. Nakkala, R. Mata and S. R. Sadras, *Process Saf. Environ. Prot.*, 2016, **100**, 288–294.
45 E. M. Ezz elregal, M. A. Ahmed, M. F. Abdel-Messih and Z. M. Abou-Gamra, *Opt. Mater.*, 2021, **111**, 110597.
46 L. Fu and Z. Fu, *Ceram. Int.*, 2015, **41**, 2492–2496.
47 M. Aliannezhadi, S. Z. Mirsanaee, M. Jamali and F. Shariatmadar Tehrani, *Sci. Rep.*, 2024, **14**, 2035.
48 I. Musa, N. Qamhieh and S. T. Mahmoud, *Results Phys.*, 2017, **7**, 3552–3556.
49 K. L. Foo, U. Hashim, K. Muhammad and C. H. Voon, *Nanoscale Res. Lett.*, 2014, **9**, 429.
50 M. S. Geetha, H. Nagabhushana and H. N. Shivananjaiah, *J. Sci.: Adv. Mater. Devices*, 2016, **1**, 301–310.
51 Z. Abbas, C. Labbez, S. Nordholm and E. Ahlberg, *J. Phys. Chem. C*, 2008, **112**, 5715–5723.
52 H. Agarwal and V. K. Shanmugam, *J. Drug Delivery Sci. Technol.*, 2019, **54**, 101291.
53 M. A. Albo Hay Allah and H. A. Alshamsi, *Biomass Convers. Biorefin.*, 2024, **14**, 10487–10500.
54 J.-A. Quek, J.-C. Sin, S.-M. Lam, A. R. Mohamed and H. Zeng, *J. Mater. Sci.: Mater. Electron.*, 2020, **31**, 1144–1158.
55 D. Suresh, P. C. Nethravathi, H. Rajanaika, H. Nagabhushana and S. C. Sharma, *Mater. Sci. Semicond. Process.*, 2015, **31**, 446–454.
56 N. Elavarasan, K. Kokila, G. Inbasekar and V. Sujatha, *Res. Chem. Intermed.*, 2017, **43**, 3361–3376.
57 Y. Gao, D. Xu, D. Ren, K. Zeng and X. Wu, *LWT*, 2020, **126**, 109297.
58 S. Vasantharaj, S. Sathiyavimal, P. Senthilkumar, V. N. Kalpana, G. Rajalakshmi, M. Alsehli, A. Elfasakhany and A. Pugazhendhi, *J. Environ. Chem. Eng.*, 2021, **9**, 105772.
59 A. R. Prasad, J. Garvasis, S. K. Oruvil and A. Joseph, *J. Phys. Chem. Solids*, 2019, **127**, 265–274.
60 S. Faisal, H. Jan, S. A. Shah, S. Shah, A. Khan, M. T. Akbar, M. Rizwan, F. Jan, Wajidullah, N. Akhtar, A. Khattak and S. Syed, *ACS Omega*, 2021, **6**, 9709–9722.
61 J. Singh, S. Kumar, A. Alok, S. K. Upadhyay, M. Rawat, D. C. W. Tsang, N. Bolan and K.-H. Kim, *J. Cleaner Prod.*, 2019, **214**, 1061–1070.
62 P. Rajiv, S. Rajeshwari and R. Venckatesh, *Spectrochim. Acta, Part A*, 2013, **112**, 384–387.
63 V. Seerangaraj, S. Sathiyavimal, S. N. Shankar, J. G. T. Nandagopal, P. Balashanmugam, F. A. Al-Misned, M. Shanmugavel, P. Senthilkumar and A. Pugazhendhi, *J. Environ. Chem. Eng.*, 2021, **9**, 105088.
64 Z. Ali, M. Aadil, B. Zainab, M. H. Rasool, W. Hassan, S. Mubarik, Z. Ahmad, N. A. Almuhous, A. A. Alothman and M. Hussain, *Inorg. Chem. Commun.*, 2023, **157**, 111399.
65 Abdullah, T. Hussain, S. Faisal, M. Rizwan, Saira, N. Zaman, M. Iqbal, A. Iqbal and Z. Ali, *J. Saudi Chem. Soc.*, 2022, **26**, 101486.
66 S. Sathiyavimal, S. Vasantharaj, D. Bharathi, M. Saravanan, E. Manikandan, S. S. Kumar and A. Pugazhendhi, *J. Photochem. Photobiol., B*, 2018, **188**, 126–134.
67 J. Puneetha, N. Kottam and A. Rathna, *Inorg. Chem. Commun.*, 2021, **125**, 108460.
68 S. Sasi, P. H. Fathima Fasna, T. K. Bindu Sharmila, C. S. Julie Chandra, J. V. Antony, V. Raman, A. B. Nair and H. N. Ramanathan, *J. Alloys Compd.*, 2022, **924**, 166431.
69 P. Kumar, M. R. Ramesh, M. Doddamani, J. Suresh and R. Lingaraj, *Mater. Lett.*, 2024, **359**, 135918.
70 S. Shabbir Awan, R. Taj Khan, A. Mehmood, M. Hafeez, S. Rizwan Abass, M. Nazir and M. Raffi, *Saudi J. Biol. Sci.*, 2023, **30**, 103487.
71 S. Dhiman, A. Kumari, A. Sharma, A. Kandwal and R. Sharma, *Inorg. Chem. Commun.*, 2024, **161**, 112088.
72 B. Şahin, R. Aydin, S. Soylu, M. Türkmen, M. Kara, A. Akkaya, H. Çetin and E. Ayyıldız, *Inorg. Chem. Commun.*, 2022, **135**, 109088.
73 S. Samar, A. Kumar and P. Kumar, *Mater. Sci. Eng., B*, 2024, **299**, 117005.
74 S. Paisoonsin, O. Pornsunthorntawee and R. Rujiravanit, *Appl. Surf. Sci.*, 2013, **273**, 824–835.
75 P. Kanmani and J.-W. Rhim, *Carbohydr. Polym.*, 2014, **106**, 190–199.
76 K. Rambabu, G. Bharath, F. Banat and P. L. Show, *J. Hazard. Mater.*, 2021, **402**, 123560.
77 S. Z. Razavi, E. Saljoughi, S. M. Mousavi and M. M. Matin, *Int. J. Biol. Macromol.*, 2024, **256**, 128090.
78 H. Mohd Yusof, N. Abdul Rahman, R. Mohamad, U. H. Zaidan and A. A. Samsudin, *OpenNano*, 2022, **8**, 100106.